JOURNAL OF GEOPHYSICAL RESEARCH: SOLID EARTH, VOL. 118, 2333–2346, doi:10.1002/jgrb.50191, 2013

Lithosphere structure and thickness beneath the North China Craton from joint inversion of ambient noise and surface wave tomography

Youcai Tang,[1] Y. John Chen,[1] Shiyong Zhou,[1] Jieyuan Ning,[1] and Zhifeng Ding[2]

Received 25 July 2012; revised 8 April 2013; accepted 9 April 2013; published 28 May 2013.

[1] We imaged detailed 3-D crustal and uppermost mantle seismic structures in the North China Craton from inversion of Rayleigh wave phase velocity at periods of 6 to 143 s. The phase velocities were obtained from a combination of ambient noise and teleseismic surface wave tomography, and then the phase velocities were inverted to *S*-wave velocities. The results show that both the Huabei Basin and Ordos Block have markedly rapid variations in both crustal velocities and the Moho depth. Huabei Basin has a thin (31–34 km) crust with low velocities while Ordos Block has a thick (~40 km) crust with high velocities. We also estimated the lithospheric thickness from the inverted *S*-wave velocities using a simple *S*-wave velocity/temperature relationship. Huabei Basin was imaged as a low *S*-wave-velocity anomaly in the uppermost mantle with very thin lithosphere (~65 km), while Ordos Block was revealed as a high *S*-wave-velocity anomaly with rather thick lithosphere (>120 km). These results indicated that Huabei Basin and Ordos Block have different thermal and/or chemical properties and had experienced different mantle processes and evolution histories since the Cenozoic. Furthermore, slow *S*-wave velocities and very thin lithosphere (~65 km) were also found beneath Hetao and Weihe rifts bounding Ordos Block at north and south, respectively. However, Shanxi Rift—the boundary between Huabei Basin and Ordos Block—had a much thicker and higher velocity lithosphere than Hetao and Weihe rifts.

Citation: Tang, Y., Y. J. Chen, S. Zhou, J. Ning, and Z. Ding (2013), Lithosphere structure and thickness beneath the North China Craton from joint inversion of ambient noise and surface wave tomography, *J. Geophys. Res. Solid Earth*, *118*, 2333–2346, doi:10.1002/jgrb.50191.

1. Introduction

[2] The North China Craton (NCC) in eastern Asia is characterized by active intraplate continental rifts and widespread magmatism in an extensional regime [*Zhang et al.*, 1998, 2003] (Figure 1). The widespread rifts and basaltic magmatism in the NCC through the Cenozoic [*Tian et al.*, 1992; *Ye et al.*, 1987] were believed to be associated with the India-Asia collision and the subduction of the Philippine Plate and the Pacific Plate beneath Eurasia [*Liu et al.*, 2004b; *Molnar and Tapponnier*, 1975; *Northrup et al.*, 1995; *Tapponnier and Molnar*, 1977; *Zhang et al.*, 2003]. Furthermore, the NCC is thought to play an important role in accommodating the interaction between the uplifting of Tibet Plateau driven by the India-Asia collision and the subduction of the Pacific Plate.

[1]Institute of Theoretical and Applied Geophysics (ITAG), School of Earth and Space Sciences, Peking University, Beijing, China.

[2]Institute of Geophysics, China Earthquake Administration, Beijing, China.

Corresponding author: Y. J. Chen, Institute of Theoretical and Applied Geophysics (ITAG), School of Earth and Space Sciences, Peking University, Beijing 100871, China. (johnyc@pku.edu.cn)

2169-9313/13/10.1002/jgrb.50191

[3] The North China Craton can be divided into the eastern (Huabei Basin) and the western block (Ordos Block), separated by a major boundary zone, the Trans-North China Orogen (TNCO), including both Shanxi Rift and Taihang Uplift (Figure 1) [*Faure et al.*, 2007; *Liu et al.*, 2006; *Zhao et al.*, 2001]. It is well known that Ordos Block has been a stable continental craton since the Precambrian amalgamation, while Huabei Basin has experienced significant tectonic rejuvenation and extension in the Late Mesozoic to Cenozoic.

[4] A number of studies using various geophysical techniques have been conducted for the region, such as receiver functions [*Chen et al.*, 2009; *Ma and Zhou*, 2007], body wave tomographies [*Huang and Zhao*, 2006; *Liu et al.*, 2004a, 2004b; *Sun and Toksoz*, 2006; *Tian et al.*, 2009; *Xu and Zhao*, 2009; *Zhao et al.*, 2009], surface wave tomographies [*He et al.*, 2009; *Huang et al.*, 2003, 2009; *Wu et al.*, 1997], ambient noise tomographies [*Fang et al.*, 2009; *Zheng et al.*, 2008a], and anisotropy analysis [*Wu et al.*, 2007; *Zhao et al.*, 2007, 2008]. These studies revealed detailed structures within the NCC. However, there are still a number of issues that need further detailed study, such as the high resolution of the seismic velocity structures and the thickness of the crust and the lithosphere, the process of the lithospheric rejuvenation and delamination of the NCC, and the relationship between the widespread rifts and extension in the NCC and the uplifting of the Tibetan Plateau.

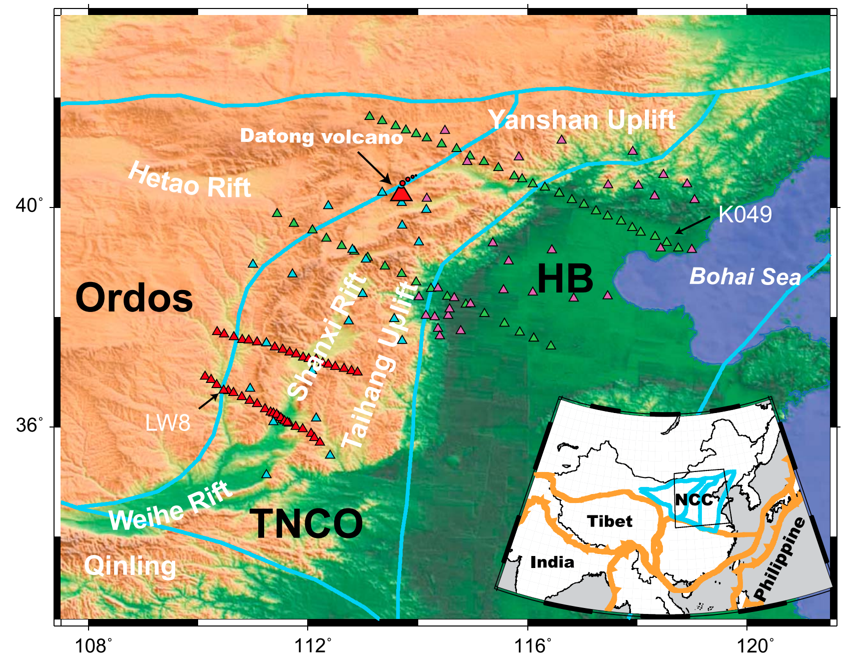

Figure 1. Tectonic settings in the North China Craton (NCC). Triangles are seismic stations, red: portable stations from Peking University, green: portable stations of Institute of Geophysics, China Earthquake Administration (CEA), blue: permanent stations from Shanxi Seismological Bureau, CEA, and purple: permanent stations from Hebei Seismological Bureau. Datong volcano is also marked as a red symbol. Blue lines denote the boundaries of and in the NCC. HB: Huabei Basin, and TNCO: Trans-North China Orogen.

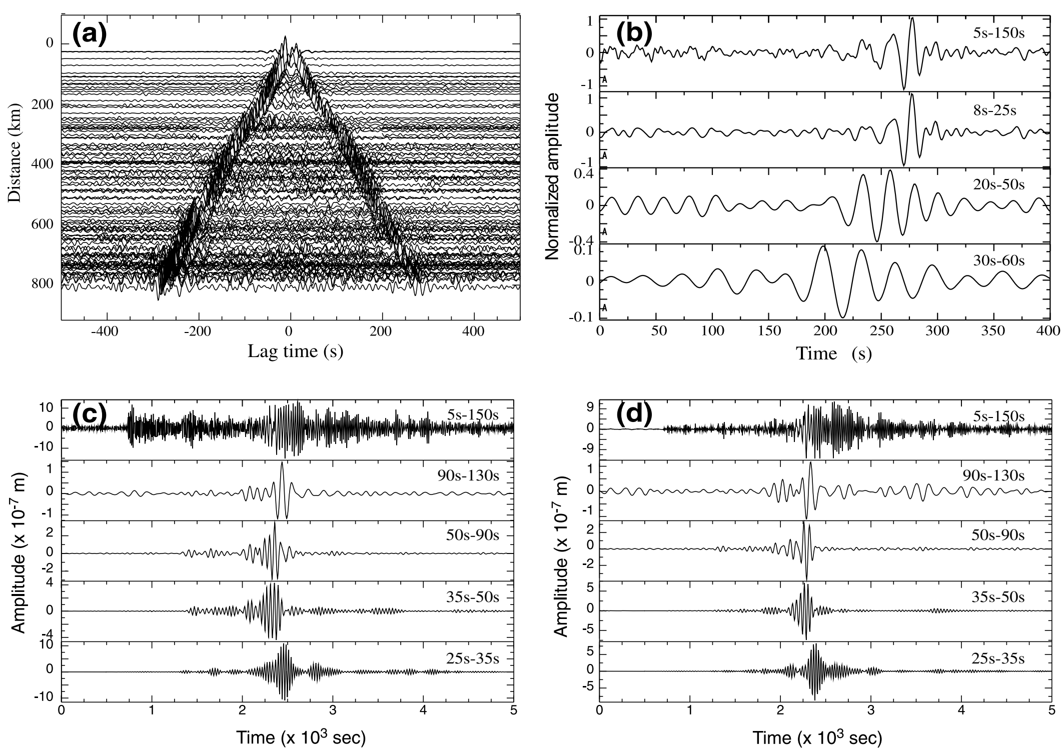

Figure 2. (a) All the cross-correlations functions used in this study; (b) an example of the cross-correlation between LW8 and K049 (Figure 1) filtered in different frequency bands; (c and d) an example of Rayleigh waves (Earthquake: JUL 27 (208), 2007, 14:46:26.800) recorded by station LW8 and K049 (Figure 1), respectively, which filtered in some frequency bands.

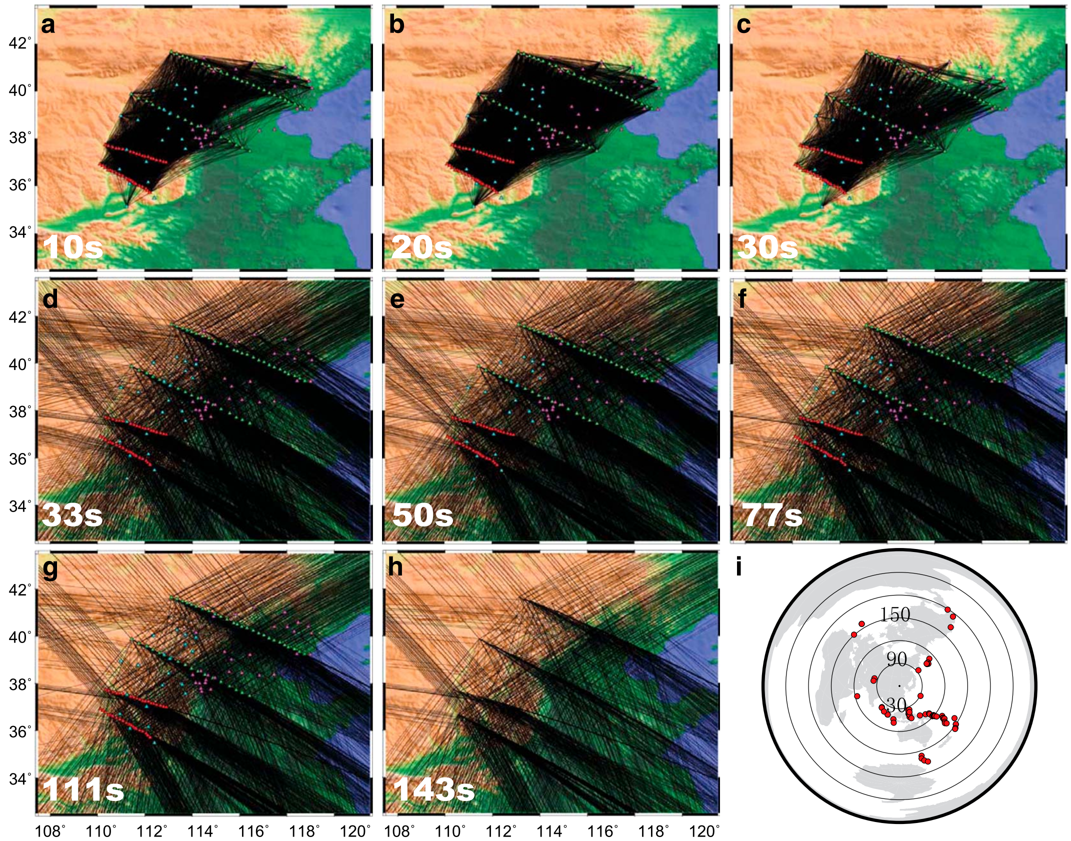

Figure 3. Raypath coverage for (a, b, c) ambient noise tomography and (d, e, f, g, h) two-plane-wave tomography at different periods, (i) earthquake distribution (red circles) for two-plane-wave tomography. Triangles are seismic arrays (see Figure 1).

[5] In this study, we used the combination of ambient noise and teleseismic surface wave tomographies to obtain detailed 3-D seismic structures in the NCC, where unprecedented seismic data were recorded by high-density and well-distributed seismic arrays. The combination of both ambient noise and teleseismic surface wave tomographies can lead to a better depth and spatial resolution of seismic structures and has enabled us to establish a detailed 3-D velocity model of the seismic structure in the NCC. These results will help us to define the rejuvenation of the NCC as well as its interaction with surrounding plates.

2. Data and Methodology

2.1. Data

[6] We used Rayleigh waves to compute tomographic phase velocity maps at set periods and then inverted these maps to obtain a 3-D *S*-wave velocity model. The phase velocities were measured from one-year continuous seismic records in 2007 at a total of 141 stations in the study region, which provided us excellent data coverage over a wide period range. The seismic data were collected from a variety of projects, including temporary and permanent seismic arrays (Figure 1).

[7] The one-year continuous data were collected from two parallel portable broadband seismic arrays that were operated by Peking University (red triangles in Figure 1). The southern array was operated for a period of 20 months from August 2006 to March 2008. Each station was equipped with a Guralp CMG-3ESP seismometer and a Reftek 130 digital acquisition system. The average station spacing was ~10 km. The northern array was operated for a period of 14 months from January 2007 to March 2008 and was composed of 13 Guralp CMG-3ESPC and 6 BKD-2 broadband seismometers.

[8] This study also included one-year continuous records during 2007 at selected stations of the two main linear profiles (green triangles in Figure 1) of the North China Seismic Array operated by the Institute of Geophysics, China Earthquake Administration (CEA). Each station was equipped with a Guralp CMG-3ESPC seismometer and a Reftek 130 digital acquisition system. More detailed information about the North China Seismic Array deployment can be found in *Lu et al.* [2009].

[9] We also collected continuous seismic records for 2007 at permanent stations from the Hebei Seismological Bureau (purple triangles in Figure 1) and the Shanxi Seismological Bureau (blue triangles in Figure 1), CEA, China. The permanent stations were equipped with a variety of sensors including broadband and short period seismographs. The short period data were not used in this study.

2.2. Methodology

[10] We obtained phase velocities of Rayleigh waves at short periods from cross-correlations of ambient noise and phase velocities at longer periods from teleseismic earthquakes. These phase velocities at shorter and longer-ranged

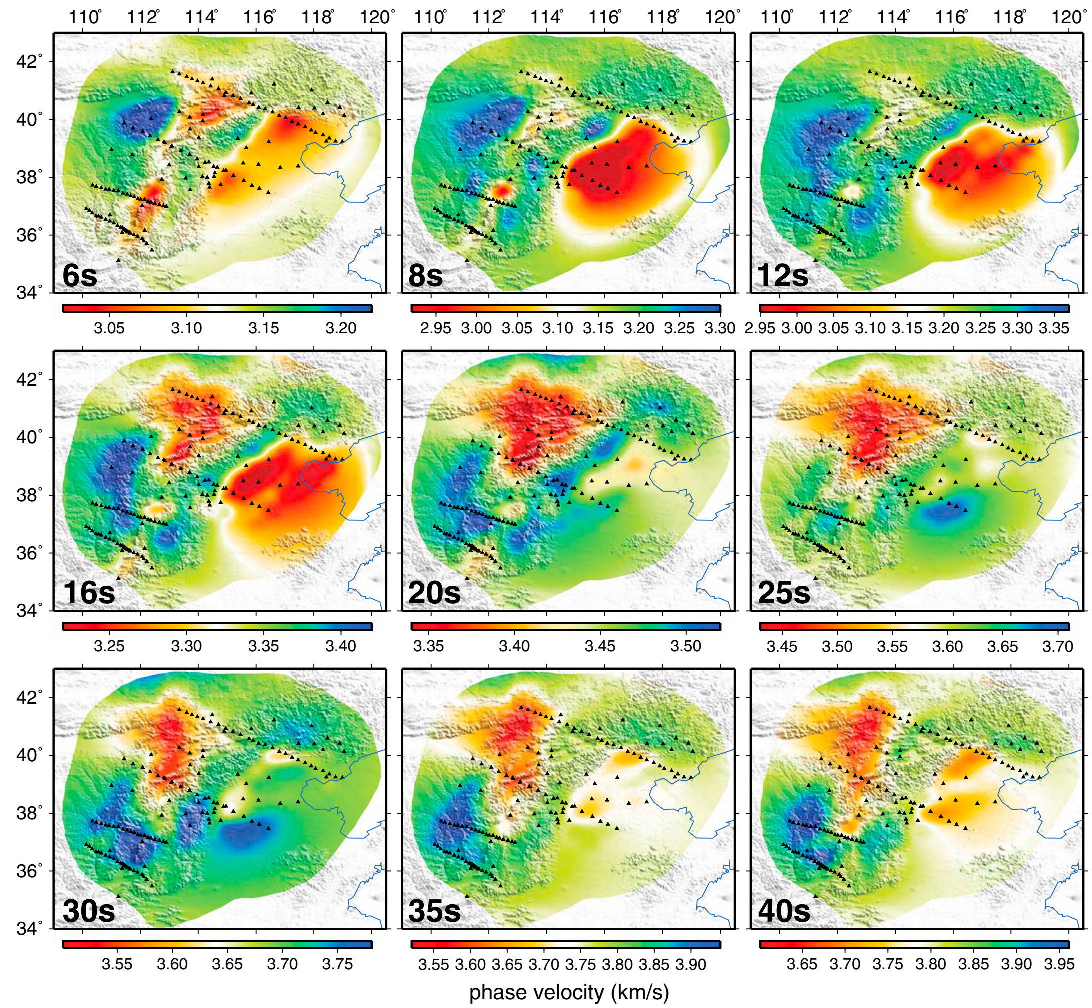

Figure 4. Phase velocity perturbation maps at different periods from ambient noise tomography. Seismic stations are shown as little black triangles.

periods were combined and inverted to *S*-wave velocities at each grid point. By assembling these results, we produced a detailed 3-D *S*-wave velocity model of the crust and the uppermost mantle in the North China Craton.

2.2.1. Ambient Noise Tomography

[11] Since *Campillo and Paul* [2003] first introduced the cross-correlation method into seismological studies, the ambient noise tomography method has become one powerful tool to image shallow Earth structures [*Shapiro and Campillo*, 2004; *Shapiro et al*., 2005]. We can obtain empirical Green's function of surface waves between pairs of stations at periods as short as 6 s by using cross-correlation of long-time sequences of ambient noise [*Bensen et al*., 2007].

[12] In this study, we performed cross-correlations of long-time sequences of ambient noise (only vertical component) over a period of 1 year for every station-pair in our seismic arrays, following the method of *Bensen et al.* [2007]. First, we removed the instrument response for each individual station and then applied a band-pass filter (0.02–0.2 Hz). Then, the time-domain normalization was applied to the data to suppress earthquake signals. Finally, we applied the spectral whitening before cross-correlating the signals. Figure 2a shows all cross-correlation functions used in this study. Figure 2b shows an example of the cross-correlation between LW8 and K049 (Figure 1) filtered in different frequency bands. Then the phase velocities for Rayleigh waves were measured from these cross-correlations between all station-pairs at periods from 6 to 40 s. Dispersion at periods longer than 40 s could not be retained from ambient noise cross-correlations for the distribution of seismic stations in this study. This is because only those station-pairs in which separation distance was greater than three wavelengths could be used.

[13] Once we obtained the dispersions at all station-pairs, conventional surface wave tomography was conducted to generate phase velocity maps at a grid size of $0.5° \times 0.5°$ by applying the method of *Barmin et al.* [2001]. The studied region was delimited by a closed curve on a sphere. Grid nodes were spaced at constant distances (~ 55 km). Surface waves were treated as rays sampling an infinitesimal zone along the great circle, while scattering was completely ignored. Spatial smoothness and model amplitude constraints were applied to the inversion for stability. Figures 3a–3c show the path coverage at several selected periods used in the tomography. All paths were located within the seismic array.

2.2.2. Two-Plane-Wave Tomography

[14] We adopted the two-plane-wave method [*Forsyth and Li*, 2005; *Forsyth et al*., 1998] for the tomography of teleseismic surface waves, which can account for the

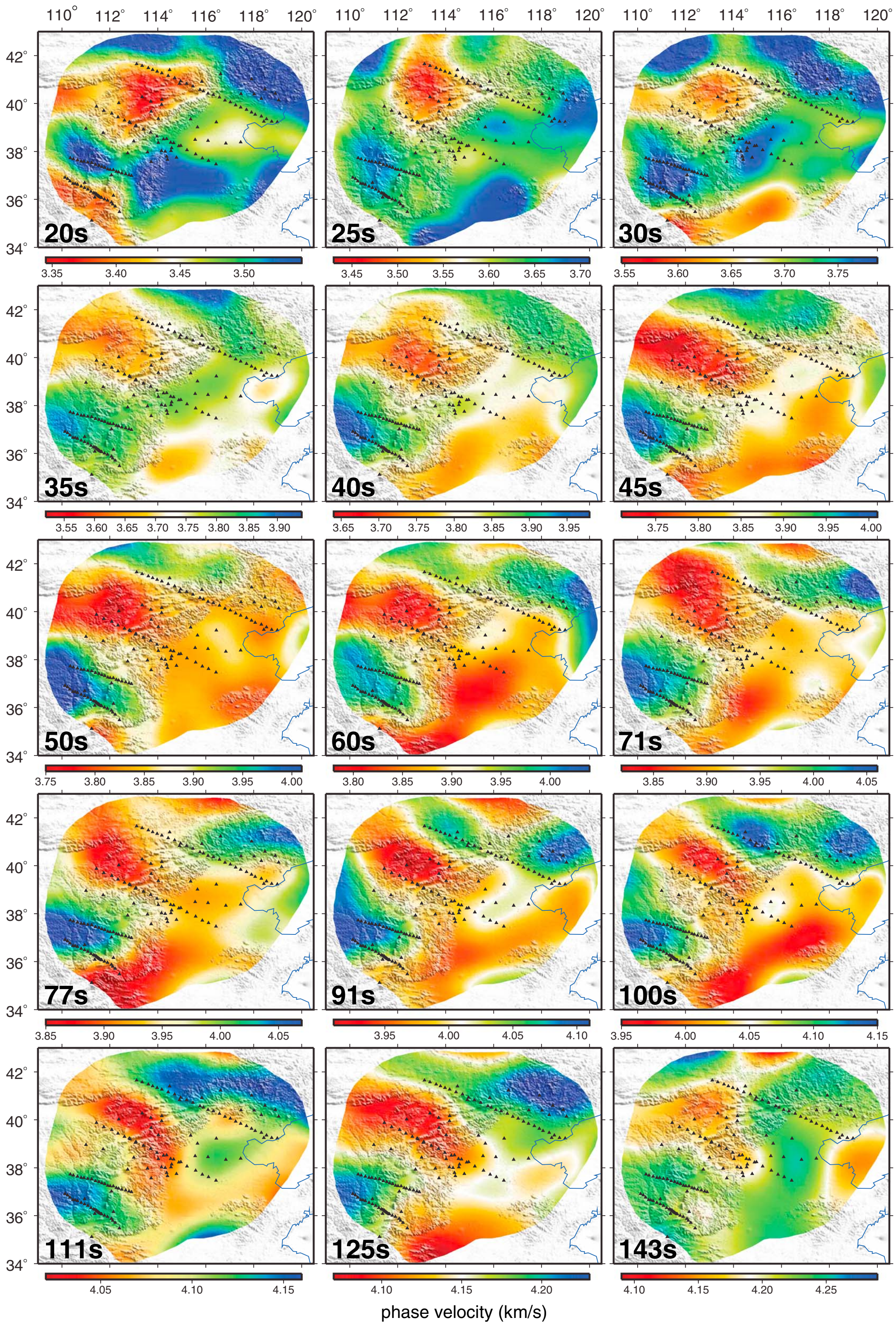

Figure 5. Phase velocity perturbation maps at different periods from two-plane-wave tomography. Only those regions whose standard errors are less than 0.08 km/s are plotted. Seismic stations are shown as little black triangles.

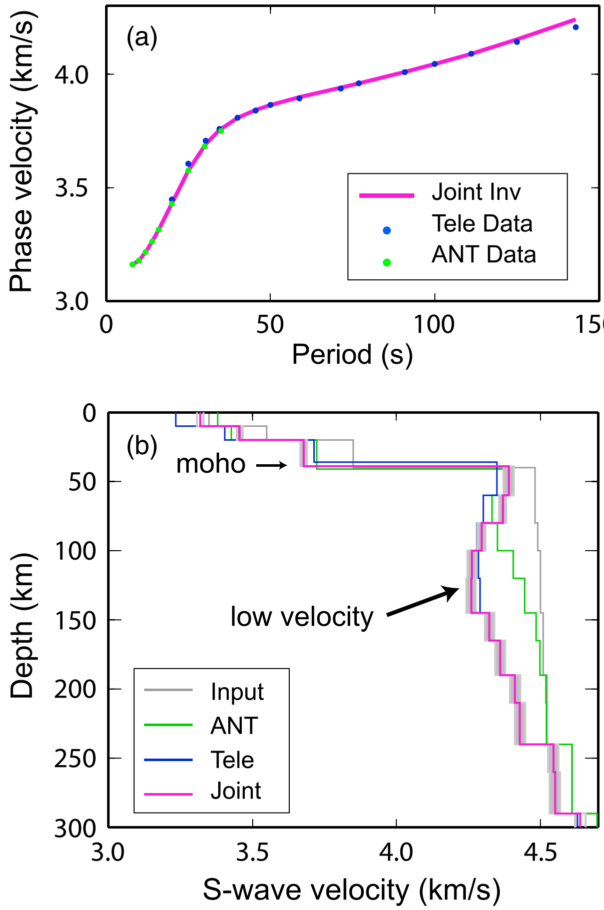

Figure 6. (a) Phase velocity dispersion curves of observed and synthetic data. ANT Data: phase velocities from ambient noise tomography, Tele Data: phase velocities form two-plane-wave tomography using teleseismic surface waves, Joint Inv: synthetic phase velocities from the inverted *S*-wave velocity model. (b) Average 1-D *S*-wave velocity in the North China Craton inverted from the combination of average phase velocities from ambient noise tomography and two-plane-wave tomography. Input: Input velocity model modified from AK135, The blue gray line denotes the standard error of the inverted *S*-wave velocity model.

incoming nonplanar wave field [*Forsyth and Li*, 2005; *Li et al.*, 2003] caused by lateral heterogeneities in the Earth's structures [*Friederich et al.*, 1994]. This method interpreted the variation in amplitude and phase of surface waves within the array in terms of the interference of two plane waves. In this study, we applied the inversion technique of surface wave tomography based on 2-D sensitivity kernels [*Yang and Forsyth*, 2006] at a grid size of 0.5° × 0.5°. We fit the observed phases and amplitudes of surface waves to get phase velocity maps at periods of 20 to 143 s. These phase velocities were then inverted to *S*-wave velocities.

[15] Earthquakes in a distance range of 30°–120° with surface wave magnitude larger than 6.0 were used in this study to isolate the fundamental mode Rayleigh waves. The distribution of these events offered a good azimuthal coverage (Figure 3i), which was important to resolve lateral variations in seismic velocity structures. The ray-path coverage is shown in Figures 3d–3h at some typical periods. Rayleigh waves were isolated independently from the vertical components at 11 selected periods, ranging from 20 to 143 s, using a zero-phase-shift band-pass Butterworth filter of 10 mHz wide. Figures 2c and 2d show an example of Rayleigh waves in some frequency bands (Earthquake: JUL 27 (208), 2007, 14:46:26.800) recorded by station LW8 and K049 (Figure 1). At a certain frequency band, only those seismograms with good signal-to-noise ratio and reasonable coherence from station to station at more than 12 stations were used in the tomography. The amplitude and phase of each Rayleigh record were calculated and were used as the input-observed data in the tomography. There was little energy at periods shorter than 20 s because of scattering and attenuation along the long path from earthquakes to the array. Information for periods longer than 143 s was limited by the period range of seismographs.

2.2.3. *S*-Wave Velocity Inversion

[16] The phase velocity maps from ambient noise and teleseismic Rayleigh waves were combined to form wide-period-band dispersion curves of 6 to 143 s. These dispersion curves were then inverted to *S*-wave velocities in the crust and in the uppermost mantle. We first performed a linear inversion for the average dispersion to get an appropriate 1-D reference *S*-wave velocity model for the entire region of interest. Then we modified the 1-D velocity model with Moho depth from receiver functions [*Ge et al.*, 2011] at each 0.5° × 0.5° grid point. These modified 1-D models were used as the initial models, which were more appropriate to the tectonic regions. We applied the same 1-D inversion procedure at each grid point and then assembled the results at all grid points together to produce one 3-D crust/uppermost mantle model.

[17] The 1-D inversion for *S*-wave velocities was performed in a linearized regime to compute the synthetic phase velocities and partial derivatives [*Saito*, 1988]. The model parameters in this inversion were *S*-wave velocities in a number of layers from the surface to 400 km depth with a prescribed layer thickness of 10–30 km. The *P*-wave velocities were scaled by a factor of 1.732 with the *S*-wave velocities and the densities were scalded with *P*-wave velocities using the same relationship as PREM in the inversion procedure. The Moho depth was inverted simultaneously by varying the thickness of the two layers right above and below the Moho to accommodate the variation in Moho depth. We used the Moho depth from receiver functions [*Ge et al.*, 2011] as the input model and updated the variation in the Moho depth during the inversion procedure. A larger damping factor was applied in the Moho depth variation to ensure that the receiver function results had strong constraints while the inversion could also allow variations in the Moho depth. For the inversion, we used the phase velocities from ambient noise tomography for the short periods and the teleseismic surface waves for longer periods. At the overlap periods, we used the average phase velocities of the two methods.

3. Results

3.1. Phase Velocity Maps

[18] Figure 4 shows the phase velocity anomalies at some selected periods ranging from 6 to 40 s from the ambient noise tomography (ANT) and Figure 5 shows the phase velocity anomalies from the two-plane-wave tomography (TPWT) for the teleseismic surface waves.

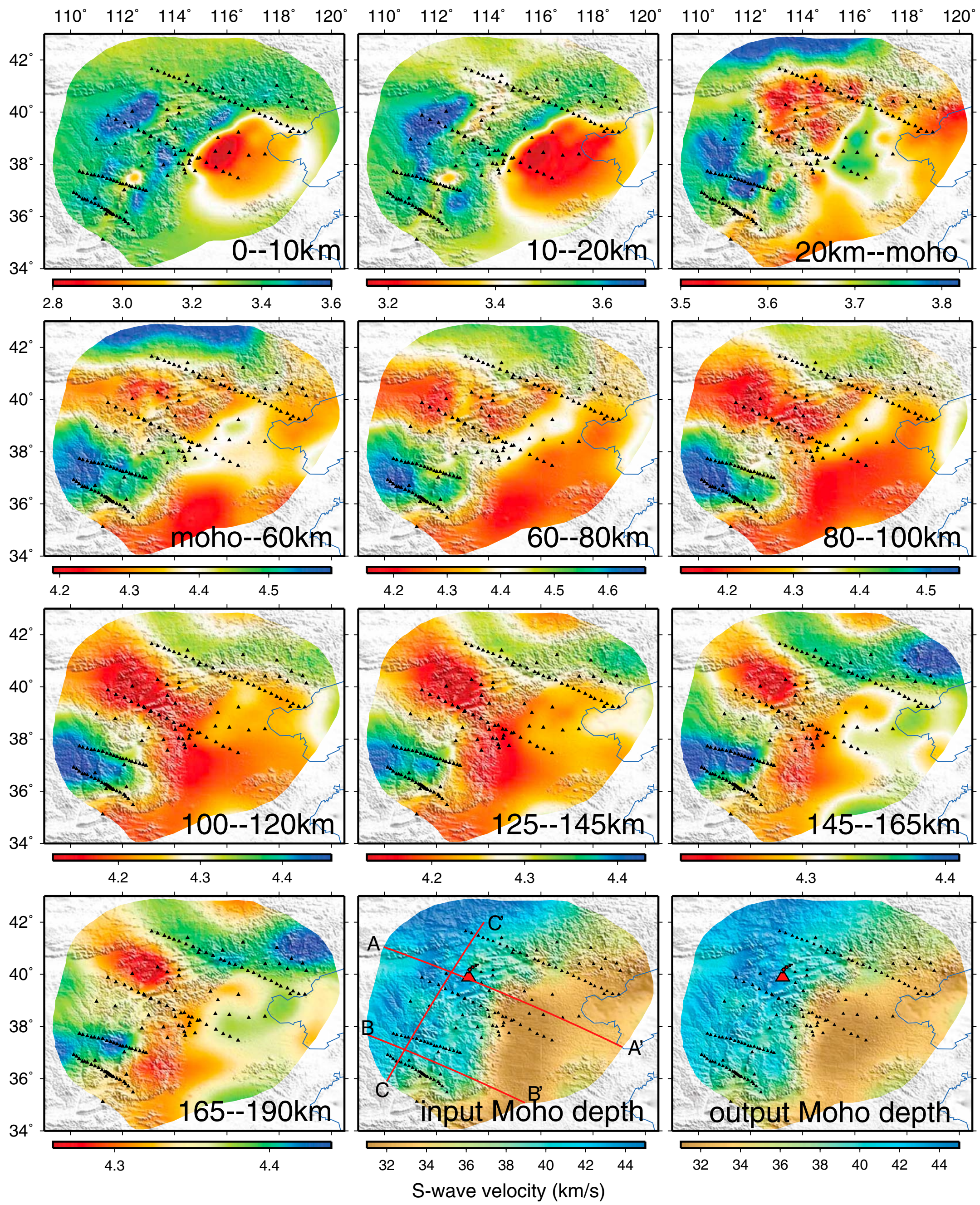

Figure 7. *S*-wave velocity anomaly maps at different depth inverted from phase velocity dispersion and Moho depth. The Moho depth is also inverted simultaneously with *S*-wave velocity. The output Moho depth is almost the same as the input Moho depth from receiver functions [*Ge et al*., 2011] because we used a large damping factor for Moho depth. Black triangles are seismic stations. The red symbol denotes the Datong volcano region.

[19] At short periods (6–16 s) (Figure 4), most of the observed velocity anomalies are well correlated with the known geological units at surface. The extensional Huabei Basin emerges as a big region with relatively low velocities. Shanxi Rift is imaged as a linear low-velocity anomaly. This linear low-velocity anomaly is limited between two high velocity anomalies beneath Ordos Block and Taihang Uplift. Ordos Block, the stable plateau to the west of Shanxi Rift, is revealed as a big region with high-velocity anomaly, contrary to Huabei Basin.

[20] The features of the phase-velocity anomaly vary gradually with periods, except the periods of 16–25 s in which depth-sensitivity kernels are maximized around the Moho. Huabei Basin is imaged as low-velocity anomaly at 16 s but changes to high-velocity anomaly at 25 s relative to Ordos Block. This striking inversion of velocity anomaly may indicate that the Moho depth beneath Huabei Basin is shallower than that of Ordos Block. In general, *S*-wave velocities are low in the crust (~3.9 km/s) and high in the upper mantle (~4.5 km/s). Consequently the phase velocities between 16 and 25 s periods

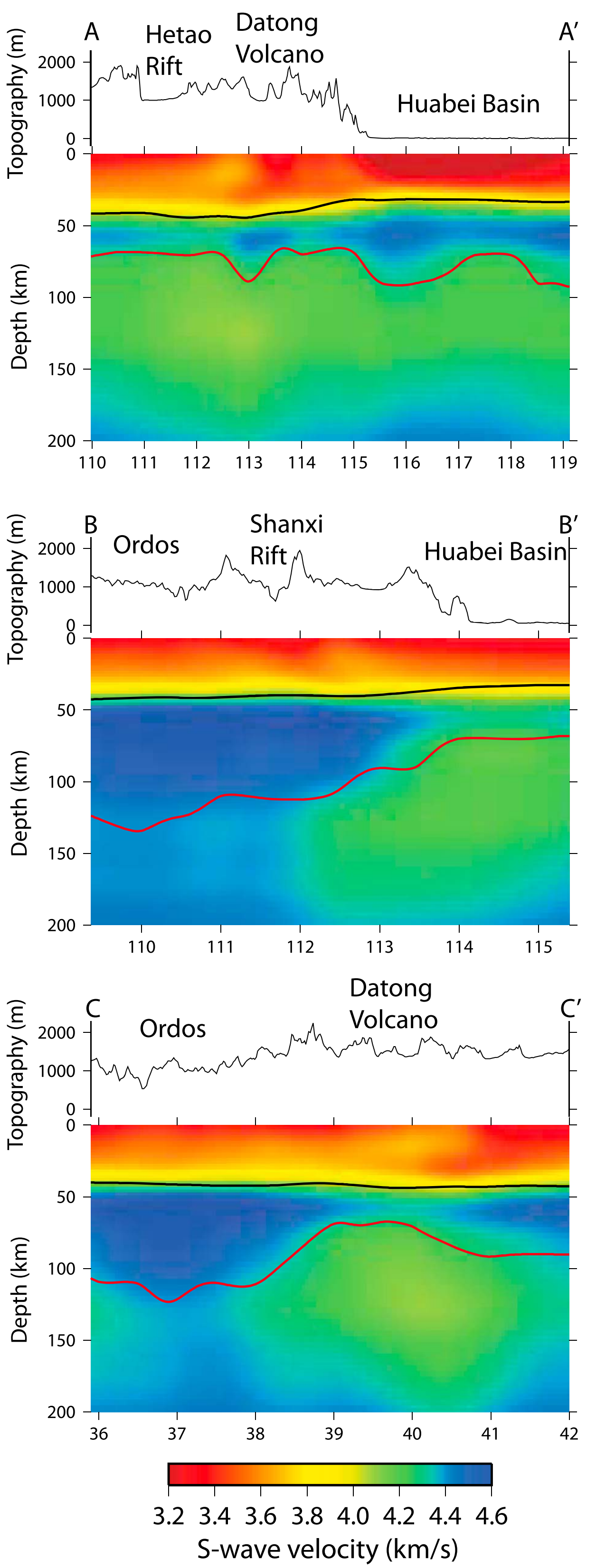

Figure 8. Vertical profiles of *S*-wave velocity structures. The locations of these profiles are marked as red lines in Figure 7. Moho depth and LAB are denoted as black and red lines, respectively.

approximately vary inversely with the crustal thickness due to the large velocity contrast (~0.6 km/s) across the Moho.

[21] The Datong volcanic region has very low velocity anomaly from short to long periods, reaching its maximum at 30–35 s periods (Figure 4). This could be due either to the thickened crust or the presence of partial melt associated with the active volcanism.

[22] At longer periods (35–40 s) (Figure 4), the phase velocities become increasingly sensitive to the lithospheric mantle structure. Ordos Block with thick craton lithospheric root emerges as a high-velocity anomaly, while Huabei Basin becomes a low-velocity anomaly where a significant portion of its lithosphere was removed.

[23] At the overlapping period range of 20–40 s, the TPWT yielded similar features (Figure 5) as that of the ANT (Figure 4). The agreement between TPWT and ANT is good where the data coverage (Figure 3) is dense for both methods, while the difference is most pronounced in lower ray-path density. There is also disagreement in the phase velocities even within the area encompassed by the seismic array. At 30–40 s periods, ANT (Figure 4) shows a high-velocity anomaly running along Taihang Mountain in the center of the seismic array. But this high-velocity anomaly shifts to the southeast in TPWT (Figure 5). The 35 and 40 s period maps are more like the 30 s period map in ANT, but they are more like 45 s period map in TPWT. These different features are probably due to the difficulty of recovering Green's functions from ambient noise at periods above 30 or 40 s [e.g., *Bensen et al.*, 2008; *Yao et al.*, 2010]. Therefore, we did not use the results from ANT at 40 s period in the inversion for *S*-wave velocity.

[24] For longer periods (>40 s), the phase velocities are more sensitive to deeper structures in the uppermost mantle. The features in the constructed phase velocity maps vary gradually with periods and exhibit similar features of 40 to 143 s. Ordos Block is revealed as a high-velocity anomaly with lower velocities at its boundaries. Strong low velocities are found beneath Huabei Basin and the rifts around Ordos Block, such as Hetao and Weihe rifts. The low velocities beneath Hetao Rift and Weihe Rift are continuous and connected to the low anomaly beneath Huabei Basin at periods of 35 to 100 s.

3.2. *S*-Wave Structure

[25] The average dispersion curves of Rayleigh wave phase velocities from ambient noise and teleseismic surface wave tomographies agree very well with each other within the overlapping periods (Figure 6a). The 1-D inversion results of *S*-wave velocities from these average phase velocities are shown in Figure 6b. The phase velocities at 6 and 40 s for ambient noise were not used in the inversion for *S*-wave velocities due to very few measurements. As expected the inverted result using only the ambient noise dispersion (shown as a green line) constrains the shallower lithosphere structure quite well. The teleseismic surface wave data, having longer periods, provides better constraint in mantle structure (shown as a blue line). The combination of ambient noise and teleseismic surface wave, therefore, is mutually complementary in *S*-wave velocity inversion with depth (shown as a purple line). The inversion requires significantly lower upper-mantle velocities from 80 to 200 km depth compared to our starting model of AK135 (Figure 6b).

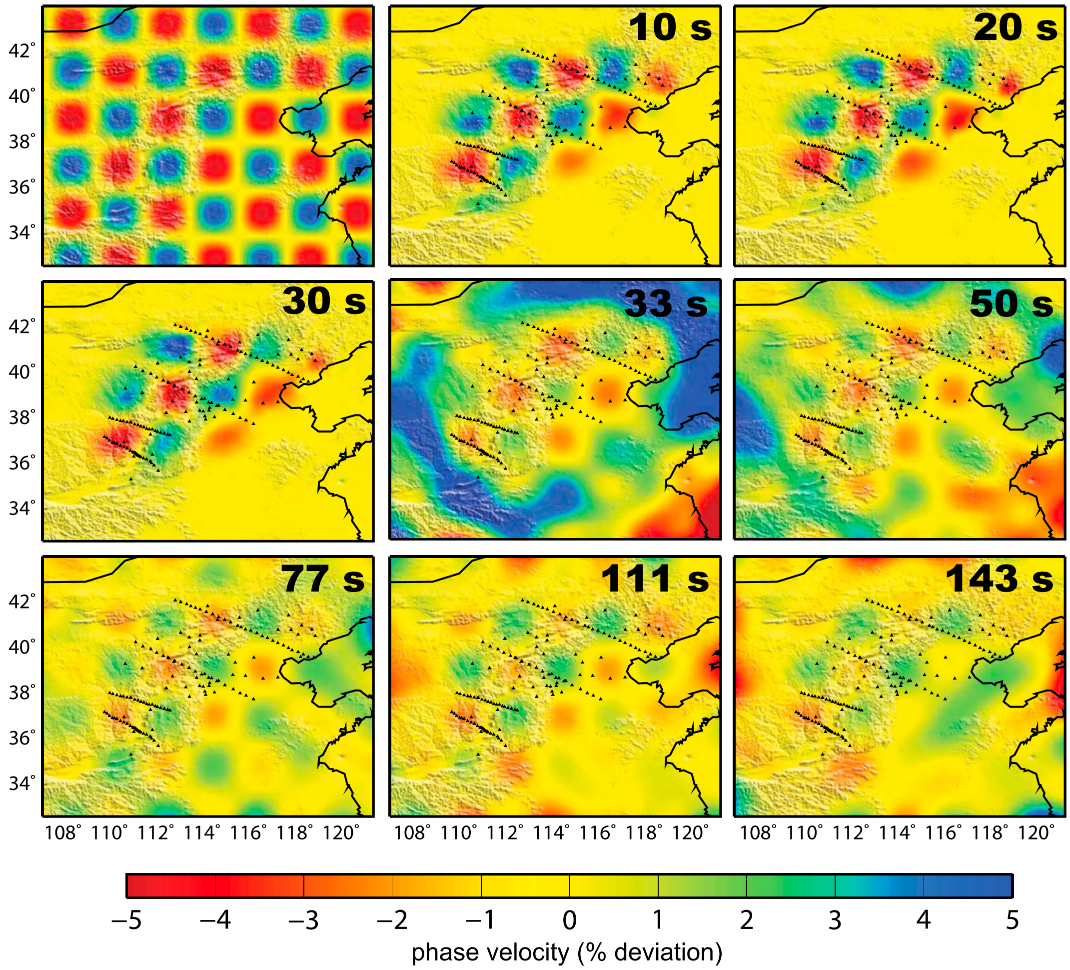

Figure 9. Results of checkerboard test. The left top panel is the input model. 10, 20, and 30 s are checkerboard tests for ambient noise tomography. 33, 50, 77, 111, and 143 s are checkerboard tests for two-plane-wave tomography. The corresponding periods are written at the right top corner on each panel.

[26] The prominent features in *S*-wave velocity maps (Figure 7) are similar to the phase velocity maps (Figures 4 and 5). In the upper and middle crust (0–10 km and 10–20 km), Huabei Basin is imaged as a strong low-velocity anomaly region. A linear low-velocity anomaly is also found beneath Shanxi rift. Ordos block and Taihang uplift are revealed as high velocity anomalies which the phase velocity maps also revealed. The *S*-wave velocity structures in the uppermost mantle down to 240 km depth also exhibit strong lateral heterogeneities. Predominantly lower shear velocities in the upper mantle beneath Huabei Basin, Hetao and Weihe rifts around Ordos are the most notable features and can be traced from the Moho to more than 200 km in depth. As expected, the stable cratonic Ordos Block is revealed as high-velocity anomaly in the uppermost mantle. The features in the mantle deeper than 200 km are not clear due to the limitation of a long period of phase dispersion and depth-sensitivity kernels.

[27] The Moho depth (Figure 7) was treated as a parameter and was inverted simultaneously with *S*-wave velocity. As we used a large dumping factor for the variation in the Moho depth, the output Moho depth is almost the same as the input Moho depth (Figure 7) from the receiver functions [*Ge et al.*, 2011]. In general, the Moho depth correlated very well with the surface tectonic features: a thinner crust beneath Huabei Basin (<34 km) and a thicker crust (>40 km) beneath TNCO and Ordos Block (Figure 11). The Datong volcanic region has an extra layer of 3–4 km lower crust as well as relatively low *S*-wave velocities.

[28] Figure 8 shows three vertical profiles of the *S*-wave velocity. The profile locations are marked as red lines in the lower middle panel in Figure 7. The lower *S*-wave velocities beneath Hetao Rift and Huabei Basin can be traced from ~70 km to more than 160 km. Ordos Block has a high velocity root down ~200 km depth.

3.3. Resolution Tests

3.3.1. Tomography

[29] Checkerboard tests were applied to check the model resolution visually. The input checkerboard is roughly 200 km in wavelength, alternating fast and slow velocity anomalies of ± 5%. Figure 9 shows the results of the recovered checkerboards at some typical periods together with the input model.

[30] The checkerboard model was well retrieved at all periods of interest for both pattern and amplitude for ANT. Given the fact that all the ray-paths were within the seismic

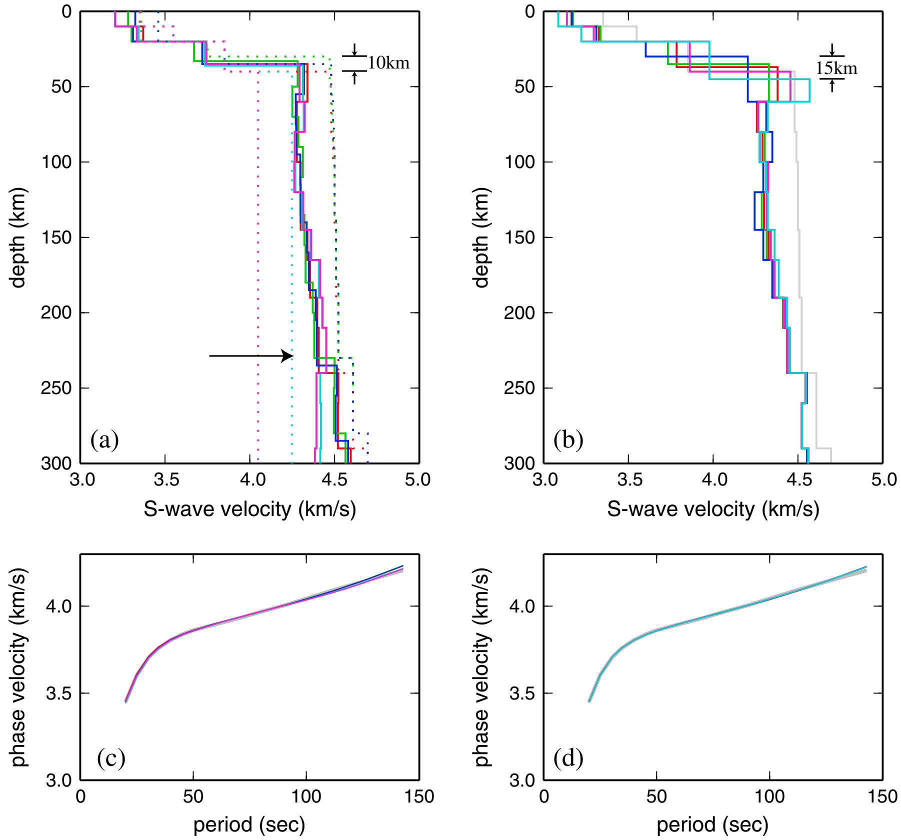

Figure 10. (a) A test of the inversion of *S*-wave velocity with different input models (dotted lines) and the results are shown with solid lines (in the same color with the input model); (b) a test of the inversion of *S*-wave velocity with different fixed Moho depth. The inverted results are plotted with different color; (c and d) the corresponding phase velocity dispersions for Figures 10a and 10b, respectively.

array (Figure 3), only the model within the array could be retrieved. So the resolution will be less than 200 km within the array for ANT inversion. Instead, we used the average phase velocity where there was no ray-path coverage/resolution for the inversion of *S*-wave velocity.

[31] The model pattern could be well recovered where the ray-path coverage was dense for teleseismic tomography. However, the retrieved amplitude is not as good as ambient noise tomography. This intrinsic shortage in amplitude retrieval for teleseismic tomography was caused by the longer-period data it used than ambient noise tomography. The checkerboard model is smeared where the path coverage shrinks and the resolution reduces gradually with periods. At 143 s, only the pattern was resolved and only ~2% velocity anomaly is recovered compared to the 5% velocity anomaly of the input model. This implies that our lateral resolution is less than 200 km where the path coverage is good and smeared where the path coverage is sparse.

3.3.2. *S*-Wave Velocity Inversion

[32] To estimate the effect of the initial model on the inversion procedure of *S*-wave velocities, we tested the inversion using some different initial models with the Moho depth varying by 10 km (Figure 10a). The different colored dotted lines are the initial models and the solid lines are the corresponding results. Figure 10c shows the corresponding phase dispersion. It is clear that all the inverted *S*-wave velocities and the Moho depths are converged above a depth of 220 km (black arrow in Figure 10a). This implies that the effect of the initial model on the inverted *S*-wave velocity is small and the maximum depth range that our phase velocity dispersion can constrain is about 220 km.

[33] Figure 10b is another test for the inversion of *S*-wave velocity to check the effect of the Moho depth. The initial models are a series of models modified from AK135 (gray line in Figure 10b) by varying the Moho depth in a range of 15 km and keeping the Moho depth fixed in the inversion procedure. The inverted *S*-wave velocity models (solid lines in Figure 10b) show that the Moho depth can significantly affect the *S*-wave velocities in the layers around the Moho. This is because the phase velocities of surface waves have a very broad sensitivity kernel with depth and have a strong trade-off between depth and velocity.

[34] We used the Moho depth from receiver functions [*Ge et al.*, 2011] as a strong constraint in the initial models. The *S*-wave velocity and the Moho depth were derived simultaneously from the inversion of the phase velocity dispersion. We used a large damping factor for the Moho depth to ensure that the receiver function results have strong constraints while the inversion can also allow variations in

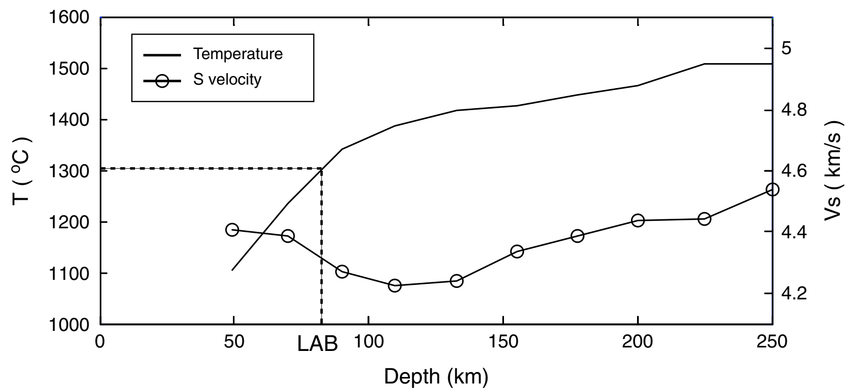

Figure 11. 1-D thermal structure of the NCC calculated from the 1-D *S*-wave velocity using formula (1). The average depth of LAB (lithosphere-asthenosphere boundary) is 86 km if we define it as a temperature boundary of 1320°C.

the Moho depth. The output Moho depth is almost the same as the input Moho depth (Figure 7).

4. Discussion

4.1. Difference Between ANT and TPWT

[35] The biggest differences between ANT and TPWT lie in the 35 and 40 s period maps. This may come from the measure error. The signals at 35 and 40 s periods have much less magnitude than 25 and 30 s period for ANT. A number of studies have shown that the Green's functions at periods above 30 or 40 s are difficult to recover from ambient noise [e.g., *Bensen et al.*, 2008]. The imperfect recovery of the Green's function above 30 s and the instable dispersion measurements are probably the primary reason for the difference between earthquake-based measurements and ambient noise-based measurements. Because of this, we did not use the results at 40 s from ambient noise in the inversion for the *S*-wave velocities.

4.2. Crust Structure

[36] Huabei Basin and Shanxi Rift have relatively low velocities in the crust than that of Ordos Block and Taihang Uplift. These low *S*-wave velocities in the crust were also

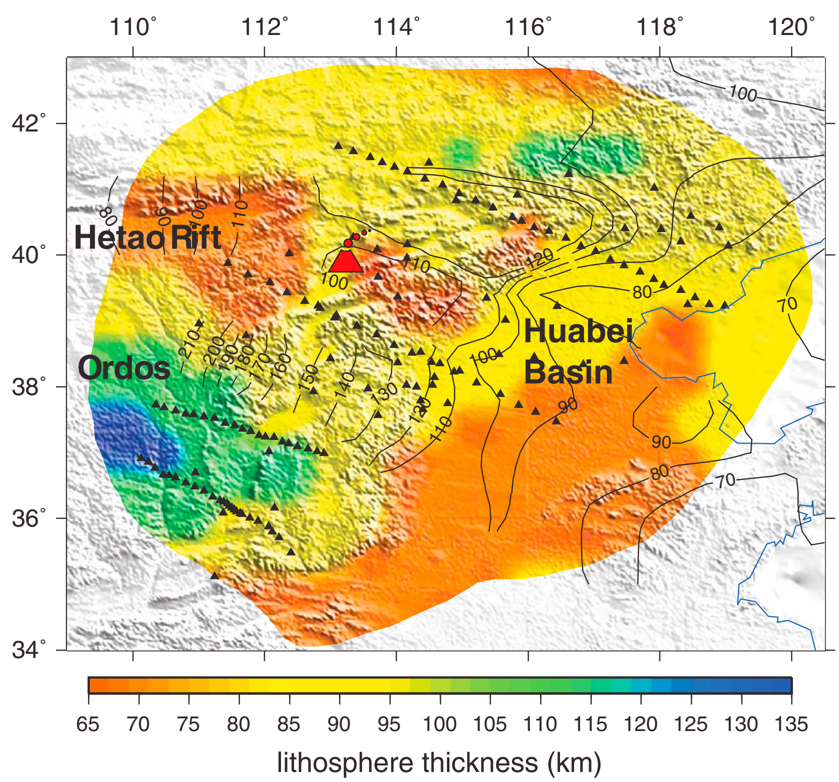

Figure 12. Thickness of Lithosphere in the NCC derived from *S*-wave velocity assume that the temperature at LAB is 1320°C. The contours are LAB depths from receiver function results [*Chen*, 2010]. Black triangles are seismic stations. Red symbol denotes the Datong volcano.

evidenced by low *Lg* coda *Q* distribution [*Liu et al*., 2004a] and low crustal *S*-wave *Q* estimate from M_L amplitude [*Wang et al*., 2008]. Given that the heat flow in Huabei Basin is high [*Hu et al*., 2000; *Wu et al*., 1988], this low velocity may indicate the existence of a hot crust beneath Huabei Basin and Shanxi Rift. This evidence may indicate that the extensional Huabei Basin and Shanxi Rift are still active now. The low velocity beneath Shanxi Rift can be traced at least to the Moho depth, indicating that the rift is lithospheric in style, cutting through the Moho. It may play an important role in accommodating the differential developing process since the Mesozoic between Huabei Basin and Ordos Block.

[37] Huabei Basin and Ordos Block have markedly rapid variations in the crustal velocities and the Moho depth along the eastern margin of Taihang Uplift. Huabei Basin has a thin and low-velocity crust while Ordos Block has a thick and high-velocity crust. The crustal thickness varies from 31–34 km beneath Huabei Basin to more than 40 km beneath TNCO and Ordos Block. These values are in good agreement with previous work such as receiver function studies [*Ma and Zhou*, 2007; *Zheng et al*., 2007, 2008b, 2008c, 2009]. The contrasting structure may indicate that Huabei Basin and Ordos Block have different thermal and/or chemical properties and have experienced different deep mantle processes and evolution histories since the Cenozoic reactivation of the NCC. These features are consistent with the notion that Huabei Basin was developed in an extensional tectonic regime [*Zhang et al*., 2003] in which its crust had been stretched and thinned significantly while Ordos Block remained stable in the Cenozoic.

[38] Low *S*-wave velocities and thick crust (43–45 km) are found near the Datong volcanic region. Considering the active volcanism evidenced by widespread Neogene basaltic outcrop near Datong [*Liu et al*., 2004b; *Xu et al*., 2005], these low *S*-wave velocities could have originated either by high temperature or partial melt in the crust, and presents a situation which is notably thermal or compositionally different. The deep Moho might be a representation of the underplating or interpenetration of the crust by melt associated with the Quaternary volcanic activities, which is also pointed out by receiver functions [*Ma and Zhou*, 2007; *Zheng et al*., 2008b] and Poisson's ratio from ultra-high pressure metamorphic rock samples [*Ji et al*., 2009].

4.3. Lithosphere Structure

[39] The velocity in the uppermost mantle is, on average, relatively slow with respect to global seismic velocity models such as AK135 (Figure 6), indicating the existence of a thinned lithosphere beneath the North China Craton. Using the *S*-wave velocities we can get an estimation of the depth of the lithosphere-asthenosphere boundary (LAB), which is thought as a thermal-controlled mechanical boundary. *Priestley and McKenzie* [2006] have obtained an empirical relationship between *S*-wave velocity (*Vs*) and temperature (Θ) in °C and depth (*z*) (equation (1)) [*Priestley and McKenzie*, 2006], based on the thermal structure of the Pacific Plate [*McKenzie et al*., 2005],

$$\begin{aligned} V_S^* &= V_S/(1 + b_V(z - 50)) \\ V_S^* &= m\Theta + c + A\exp[-(E + PV_a)/RT], \end{aligned} \tag{1}$$

where E is the activation energy, and V_a is the activation volume, T is the temperature in °K, and the constant values are

$$\begin{aligned} b_V &= 3.84 \times 10^{-4}\text{km}^{-1}, m = -2.8 \times 10^{-4}\text{km s}^{-1}\text{C}^{-1}, \\ c &= 4.72 \text{ km}s^{-1}, A = -1.8 \times 10^{13}\text{km s}^{-1}, \\ E &= 409 \text{ kJ mol}^{-1}, V_a = 10 \times 10^{-6}\text{m}^3 \text{ mol}^{-1}, \\ P &= \int \rho(z)gdz, R = 8.314472J \text{ mol}^{-1}K^{-1}. \end{aligned}$$

[40] Equation (1) provides a good fit of *Vs*(*T*) for the Pacific lithosphere. The LAB is conventionally defined as the 1300°C isotherm because mantle rocks below this temperature are sufficiently cool and behave in a rigid manner [*Karato*, 2009]. For the North China Craton, we use only the values *T*(z) that exceed to 1100°C to estimate the depth of LAB, where the continental-crustal effect will be very small.

[41] Figure 11 shows the average 1-D temperature profile estimated from the average 1-D *S*-wave velocity model using equation (1). We chose 1320°C as the typical LAB temperature in the North China Craton. The derived LAB depth in Huabei Basin was similar with the receiver function results [*Chen*, 2010]. The derived average depth of LAB in our study region is 86 km. By applying the same approach at each of the 0.5° × 0.5° grid, we got estimations of the LAB depth across the NCC.

[42] Figure 12 shows the variation in the LAB depths derived from *S*-wave velocity at 1320°C. Huabei Basin has a very shallow LAB (~60–65 km), which is consistent with the notions that part of the NCC lithosphere had been destroyed and thinned significantly before the Cenozoic. The Cenozoic rift systems surrounding the Ordos Block, such as the Hetao and Weihe rifts, also have thin lithosphere (60–65 km) similar to that of Huabei Basin. These LAB estimations agree well with previous work using other imaging techniques. Travel-time tomographies reported that the lithosphere beneath Huabei Basin is only 60–80 km [*Tian et al*., 2009; *Xu and Zhao*, 2009]. Compositional analysis of alkali basalts from the Quaternary Datong volcanic field inferred a temporal thinning of the lithosphere (~70 km) [*Xu et al*., 2005]. Our results suggest that this destruction and lithospheric thinning was not limited in Huabei Basin, but also had a more significant effect on TNCO and Ordos Block than previously thought (Figure 12).

[43] Ordos Block, as a typical Archean craton, has a thicker lithosphere (>120 km) than that of Huabei Basin and Hetao Rift (60–65 km) (Figures 8 and 12) if we used the same LAB temperature (1320°C) as Huabei Basin. However, the receiver function revealed that this LAB depth is thinner by more than 100 km, while Huabei Basin has a similar LAB depth with receiver function results (Figure 12). The LAB temperature will be 1420°C in Ordos Block to get a deep LAB (>200 km) as receiver function revealed [*Chen*, 2010]. There could be several reasons for this difference in the LAB depth or the temperature. First, equation (1) was derived from the Pacific lithosphere, which is more like the reactivated Huabei Basin. However, the Ordos Block is a stable Archean craton with a cold thick lithospheric root, which will have a much different thermal profile than the Pacific lithosphere. Second, Ordos has a much higher *S*-wave velocity structure beneath the

derived LAB than that of Huabei Basin (Figure 8). Whether this interface is a midlithosphere discontinuity, more data needs to be checked. Nevertheless, Ordos Block and Huabei Basin have marked difference in the crustal and lithospheric structures.

[44] A very thin lithosphere (<70 km) is found beneath Hetao Rift which is almost the same as Huabei Basin (Figure 12). But Shanxi Rift, though it has a linear low-velocity anomaly in the crust, does not show very thin lithosphere. These features may indicate that the rifts around the stable cratonic Ordos Block have evolved under different regime.

5. Conclusion

[45] In this study, ambient noise and teleseismic surface wave tomographies are combined to produce a detailed 3-D *S*-wave velocity model of the crust and the uppermost mantle in the North China Craton.

[46] Huabei Basin and Ordos Block have markedly rapid variations in crustal velocities and the Moho depth along the eastern margin of Taihang uplift. Huabei Basin has a thin and low-velocity crust while Ordos Block has a thick and high-velocity crust. These features may indicate different thermal and/or chemical properties, deep mantle process and evolution history between Ordos Block and Huabei Basin since the Cenozoic.

[47] Huabei Basin has a very shallow LAB (~60–65 km), which is consistent with the notion that part of the lithosphere of the North China Craton had been destroyed and thinned significantly in the Cenozoic. The Cenozoic rift systems surrounding Ordos Block, such as the Hetao and Weihe rifts, have also been significantly thinned to 60–65 km, which may indicate the destruction and lithospheric thinning was not limited to Huabei Basin, but also affected the rifts system around Ordos Block.

[48] Ordos Block has a thicker lithosphere with higher *S*-wave velocity while the rift zones around Ordos have thinner lithosphere. But Shanxi Rift, the boundary rift between Ordos Block and Huabei Basin, has much thicker lithosphere than that of Hetao and Weihe rifts.

[49] **Acknowledgments.** This work was supported by NSF China grants (90814002; 40821062). We would like to thank Yingjie Yang who supplied the software for tomography and *S*-wave velocity inversion. We also would like to thank Ling Chen to provide the LAB depth and Yong Zheng to provide Moho depth from receiver functions.

References

Barmin, M. P., M. H. Ritzwoller, and A. L. Levshin (2001), A fast and reliable method for surface wave tomography, *Pure Appl. Geophys.*, *158*(8), 1351–1375.

Bensen, G. D., M. H. Ritzwoller, M. P. Barmin, A. L. Levshin, F. Lin, M. P. Moschetti, N. M. Shapiro, and Y. Yang (2007), Processing seismic ambient noise data to obtain reliable broad-band surface wave dispersion measurements, *Geophys. J. Int.*, *169*(3), 1239–1260.

Bensen, G. D., M. H. Ritzwoller, and N. M. Shapiro (2008), Broadband ambient noise surface wave tomography across the United States, *J. Geophys. Res.*, *113*, B05306, doi:10.1029/2007JB005248.

Campillo, M., and A. Paul (2003), Long-range correlations in the diffuse seismic coda, *Science*, *299*(5606), 547–549.

Chen, L. (2010), Concordant structural variations from the surface to the base of the upper mantle in the North China Craton and its tectonic implications, *Lithos*, *120*(1–2), 96–115.

Chen, L., C. Cheng, and Z. G. Wei (2009), Seismic evidence for significant lateral variations in lithospheric thickness beneath the central and western North China Craton, *Earth Planet. Sci. Lett.*, *286*(1–2), 171–183.

Fang, L. H., J. P. Wu, and Z. Y. Lu (2009), Rayleigh wave group velocity tomography from ambient seismic noise in North China, *Chin. J. Geophys.-Chin. Edn.*, *52*(3), 663–671.

Faure, M., P. Trap, W. Lin, P. Monie, and O. Bruguier (2007), Polyorogenic evolution of the paleoproterozoic Trans-North China Belt - New insights from the Luliangshan-Hengshan-Wutaishan and Fuping massifs, *Episodes*, *30*(2), 96–107.

Forsyth, D., and A. Li (2005), Array analysis of two-dimensional variations in surface wave phase velocity and azimuthal anisotropy in the presence of multipathing interference, *Geophysical Monogr.-Am. Geophysical Union*, *157*, 81.

Forsyth, D. W., S. C. Webb, L. M. Dorman, and Y. Shen (1998), Phase velocities of Rayleigh waves in the MELT experiment on the East Pacific Rise, *Science*, *280*(5367), 1235–1238.

Friederich, W., E. Wielandt, and S. Stange (1994), Nonplane Geometries of Seismic Surface Wave-Fields and Their Implications for Regional Surface-Wave Tomography, *Geophys. J. Int.*, *119*(3), 931–948.

Ge, C., Y. Zheng, and X. Xiong (2011), Study of crustal thickness and Poisson ration of the North China Craton, *Chin. J. Geophys.-Chin.*, *54*(10), 2538–2548.

He, Z. Q., T. L. Ye, and Z. F. Ding (2009), Surface wave tomography for the phase velocity in the northeastern part of North China, *Chin. J. Geophys.-Chin. Edn.*, *52*(5), 1233–1242.

Hu, S., L. He, and J. Wang (2000), Heat flow in the continental area of China: a new data set, *Earth Planet. Sci. Lett.*, *179*(2), 407–419.

Huang, J. L., and D. P. Zhao (2006), High-resolution mantle tomography of China and surrounding regions, *J. Geophys. Res.*, *111*, B09305, doi:10.1029/2005JB004066.

Huang, Z. X., W. Su, Y. J. Peng, Y. J. Zheng, and H. Y. Li (2003), Rayleigh wave tomography of China and adjacent regions, *J. Geophys. Res.*, *108*(B2), 2073, doi:10.1029/2001JB001696.

Huang, Z. X., H. Y. Li, Y. J. Zheng, and Y. J. Peng (2009), The lithosphere of North China Craton from surface wave tomography, *Earth Planet. Sci. Lett.*, *288*(1–2), 164–173.

Ji, S. C., Q. Wang, and M. H. Salisbury (2009), Composition and tectonic evolution of the Chinese continental crust constrained by Poisson's ratio, *Tectonophysics*, *463*(1–4), 15–30.

Karato, S. (2009), On the rigin of the asthenosphere, *Earth Planet. Sci. Lett.*, *321–322*, 95–103.

Li, A. B., D. W. Forsyth, and K. M. Fischer (2003), Shear velocity structure and azimuthal anisotropy beneath eastern North America from Rayleigh wave inversion, *J. Geophys. Res.*, *108*(B8), 2362, doi:10.1029/2002JB002259.

Liu, J. H., F. T. Liu, X. W. Yan, Y. Xu, and T. Y. Hao (2004a), A study of Lg coda attenuation beneath North China: Seismic imaging of Lg coda Q (0), *Chin. J. Geophys.-Chin. Edn.*, *47*(6), 1044–1052.

Liu, M., X. J. Cui, and F. T. Liu (2004b), Cenozoic rifting and volcanism in eastern China: a mantle dynamic link to the Indo-Asian collision?, *Tectonophysics*, *393*(1–4), 29–42.

Liu, S. W., G. C. Zhao, S. A. Wilde, G. M. Shu, M. Sun, Q. G. Li, W. Tian, and J. Zhang (2006), Th-U-Pb monazite geochronology of the Luliang and Wutai Complexes: Constraints on the tectonothermal evolution of the Trans-North China Orogen, *Precambrian Res.*, *148*(3–4), 205–224.

Lu, L. Y., Z. Q. He, Z. F. Ding, and Z. X. Yao (2009), Investigation of ambient noise source in North China array, *Chinese J Geophys-En.*, *52*(5), 1053–1060.

Ma, Y. L., and H. L. Zhou (2007), Crustal thicknesses and Poisson's ratios in China by joint analysis of teleseismic receiver functions and Rayleigh wave dispersion, *Geophys. Res. Lett.*, *34*, L12304, doi:10.1029/2007GL029848.

McKenzie, D., J. Jackson, and K. Priestley (2005), Thermal structure of oceanic and continental lithosphere, *Earth Planet. Sci. Lett.*, *233*(3–4), 337–349.

Molnar, P., and P. Tapponnier (1975), Cenozoic Tectonics of Asia - Effects of a Continental Collision, *Science*, *189*(4201), 419–426.

Northrup, C. J., L. H. Royden, and B. C. Burchfiel (1995), Motion of the Pacific Plate Relative to Eurasia and Its Potential Relation to Cenozoic Extension Along the Eastern Margin of Eurasia, *Geology*, *23*(8), 719–722.

Priestley, K., and D. McKenzie (2006), The thermal structure of the lithosphere from shear wave velocities, *Earth Planet. Sci. Lett.*, *244*(1–2), 285–301.

Saito, M. (1988), DISPER80: A subroutine package for the calculation of seismic normal-mode solutions, *Seismological Algorithms: Computational Methods and Computer Programs*, 293¨C319.

Shapiro, N. M., and M. Campillo (2004), Emergence of broadband Rayleigh waves from correlations of the ambient seismic noise, *Geophys. Res. Lett.*, *31*, L07614, doi:10.1029/2004GL019491.

Shapiro, N. M., M. Campillo, L. Stehly, and M. H. Ritzwoller (2005), High-resolution surface-wave tomography from ambient seismic noise, *Science*, *307*(5715), 1615–1618.

Sun, Y. S., and M. N. Toksoz (2006), Crustal structure of China and surrounding regions from *P* wave traveltime tomography, *J. Geophys. Res.*, *111*, B03310, doi:10.1029/2005JB003962.

Tapponnier, P., and P. Molnar (1977), Active Faulting and Tectonics in China, *J. Geophys. Res.*, *82*(20), 2905–&.

Tian, Z. Y., P. Han, and K. D. Xu (1992), The Mesozoic Cenozoic East China Rift System, *Tectonophysics*, *208*(1-3), 341–363.

Tian, Y., D. P. Zhao, R. M. Sun, and J. W. Teng (2009), Seismic imaging of the crust and upper mantle beneath the North China Craton, *Phys. Earth and Planet. In.*, *172*(3–4), 169–182.

Wang, S. Y., S. P. Pei, T. M. Hearn, Z. H. Xu, J. F. Ni, and Y. X. Yu (2008), Crustal *S*-wave Q estimated from M-L amplitude II: Q lateral variation in China, *Chin. J. Geophys.-Chin. Edn.*, *51*(1), 133–139.

Wu, F. T., A. L. Levshin, and V. M. Kozhevnikov (1997), Rayleigh wave group velocity tomography of Siberia, China and the vicinity, *Pure Appl. Geophys.*, *149*(3), 447–473.

Wu, J., Y. Gao, Y. Chen, and J. Huang (2007), Seismic anisotropy in the crust in northwestern capital area of China [J], *Chinese J. Geophys.*, *50*(1), 209–220.

Wu, Q., Y. Xie, J. Zu, and D. Wang (1988), A Study on the Geothermal Field in North China, *Earthquake Res. China*, *4*(1), 41–48.

Xu, P. F., and D. P. Zhao (2009), Upper-mantle velocity structure beneath the North China Craton: implications for lithospheric thinning, *Geophys. J. Int.*, *177*(3), 1279–1283.

Xu, Y. G., J. L. Ma, F. A. Frey, M. D. Feigenson, and J. F. Liu (2005), Role of lithosphere-asthenosphere interaction in the genesis of Quaternary alkali and tholeiitic basalts from Datong, western North China Craton, *Chem. Geol.*, *224*(4), 247–271.

Yang, Y. J., and D. W. Forsyth (2006), Regional tomographic inversion of the amplitude and phase of Rayleigh waves with 2-D sensitivity kernels, *Geophys. J. Int.*, *166*(3), 1148–1160.

Yao, H., R. D. van der Hilst, and J. P. Montagner (2010), Heterogeneity and anisotropy of the lithosphere of SE Tibet from surface wave array tomography, *J. Geophys. Res.*, *115*, B12307, doi:10.1029/2009JB007142.

Ye, H., B. T. Zhang, and F. Y. Mao (1987), The Cenozoic Tectonic Evolution of the Great North China - 2 Types of Rifting and Crustal Necking in the Great North China and Their Tectonic Implications, *Tectonophysics*, *133*(3–4), 217–227.

Zhang, Y. Q., J. L. Mercier, and P. Vergely (1998), Extension in the graben systems around the Ordos (China), and its contribution to the extrusion tectonics of south China with respect to Gobi-Mongolia, *Tectonophysics*, *285*(1–2), 41–75.

Zhang, Y. Q., Y. S. Ma, N. Yang, W. Shi, and S. W. Dong (2003), Cenozoic extensional stress evolution in North China, *J.Geodynamics*, *36*(5), 591–613.

Zhao, G., S. A. Wilde, P. A. Cawood, and M. Sun (2001), Archean blocks and their boundaries in the North China Craton: lithological, geochemical, structural and P-T path constraints and tectonic evolution, *Precambrian Res.*, *107*(1–2), 45–73.

Zhao, L., T. Y. Zheng, L. Chen, and Q. S. Tang (2007), Shear wave splitting in eastern and central China: Implications for upper mantle deformation beneath continental margin, *Phys. Earth and Planet. In.*, *162*(1–2), 73–84.

Zhao, L., T. Y. Zheng, and G. Lu (2008), Insight into craton evolution: Constraints from shear wave splitting in the North China Craton, *Phys. Earth and Planet. In.*, *168*(3–4), 153–162.

Zhao, L., R. M. Allen, T. Y. Zheng, and S. H. Hung (2009), Reactivation of an Archean craton: Constraints from *P*- and *S*-wave tomography in North China, *Geophys. Res. Lett.*, *36*, L17306, doi:10.1029/2009GL039781

Zheng, T. Y., L. Chen, L. Zhao, and R. X. Zhu (2007), Crustal structure across the Yanshan belt at the northern margin of the North China Craton, *Phys. Earth and Planet. In.*, *161*(1–2), 36–49.

Zheng, S. H., X. L. Sun, X. D. Song, Y. J. Yang, and M. H. Ritzwoller (2008a), Surface wave tomography of China from ambient seismic noise correlation, *Geochem. Geophys. Geosyst.*, *9*, Q05020, doi:10.1029/2008GC001981.

Zheng, T. Y., L. Zhao, and R. X. Zhu (2008b), Insight into the geodynamics of cratonic reactivation from seismic analysis of the crust-mantle boundary, *Geophys. Res. Lett.*, *35*, L08303, doi:10.1029/2008GL033439.

Zheng, T. Y., L. Zhao, W. W. Xu, and R. X. Zhu (2008c), Insight into modification of North China Craton from seismological study in the Shandong Province, *Geophys. Res. Lett.*, *35*, L22305 doi:10.1029/2008GL035661.

Zheng, T. Y., L. Zhao, and R. X. Zhu (2009), New evidence from seismic imaging for subduction during assembly of the North China craton, *Geology*, *37*(5), 395–398.